Application of Semantic Segmentation in High-Impedance Fault Diagnosis Combined Signal Envelope and Hilbert Marginal Spectrum for Resonant Distribution Networks

Jian-Hong Gao[a,c], Mou-Fa Guo[a,*], Shuyue Lin[b], and Duan-Yu Chen[c,*]
[a] College of Electrical Engineering and Automation, Fuzhou University, Fuzhou, 350108, China
[b] School of Engineering, University of Hull, Hull, HU67RX, UK
[c] Department of Electrical Engineering, Yuan Ze University, Taoyuan 32003, Taiwan

Abstract
The diagnosis of high-impedance fault (HIF) is a critical challenge due to the presence of faint signals that exhibit distortion and randomness. In this study, we propose a novel diagnostic approach for HIF based on semantic segmentation of the signal envelope (SE) and Hilbert marginal spe)trum (HMS). The proposed approach uses 1D-UNet to identify the transient process of potential fault events in zero-sequence voltage to judge fault inception. Longer timescale zero-sequence voltage is then used to extract SE and HMS, representing HIF distortion and randomness characteristics. These features are transformed into images, and ResNet18 is employed to detect the presence of HIF. An industrial prototype of the proposed approach has been implemented and validated in a 10 kV test system. The experimental results indicate that the proposed approach outperforms the comparison by a significant margin regarding triggering deviation and detection accuracy, particularly in resonant distribution networks.

Keywords: Resonant distribution networks; single-phase ground fault; high-impedance fault diagnosis; fault triggering; fault detection; semantic segmentation; deep learning; signal envelope; Hilbert marginal spectrum.

1. Introduction

Diagnosing high-impedance faults (HIF) poses significant challenges in resonant distribution networks, particularly in outdoor settings where multiple-spurred overhead lines are prone to environmental disturbances (Guo et al., 2018). HIFs, characterized by low-level current, distortion, and randomness, are more difficult to detect than low-impedance faults (LIF) when employing conventional protection relays. Furthermore, HIFs frequently result in arc discharges, producing elevated temperatures capable of igniting proximate combustible materials and causing fires or personal injury accidents. Consequently, there is an urgent need for efficacious technical solutions to accurately diagnose HIFs, thereby mitigating risks and averting potential hazards.

In pursuit of this objective, many researchers have dedicated their efforts to devising HIF diagnostic methodologies, culminating in a proliferation of novel fault diagnosis techniques. The prevailing HIF diagnosis methods can be divided into two primary categories: threshold-based methods and artificial intelligence (AI) methods, depending on the application of a predetermined threshold.

1) Threshold-based methods (Sarwagya et al., 2018; Wang et al., 2015) have gained widespread popularity in practical engineering due to their fast response speed and straightforward logic. These methods rely on preset thresholds, such that when the instantaneous value of the raw signal exceeds the threshold, the fault inception is determined immediately. In (Wang & Cui, 2022; Wang et al., 2018), the initial polarity and profile of zero-sequence voltage and current were considered fault indicators. The summation of the accumulated difference of residual voltage was employed to distinguish fault events from non-fault events in (Biswal & Parida, 2022). A transient detection index was proposed using the Savitzky-Golay filter and matrix pencil method to secure HIF detection (Biswal et al., 2022). Based on mathematical morphology, a closing opening difference operation (CODO) was calculated to detect any disturbance in phase voltage (Gautam & Brahma, 2013). Meanwhile, wait and reset times were defined to distinguish HIF from other events. Such time-domain methods were explainable for their simple logic to construct time-domain thresholds but were vulnerable to improper frequency range selection for the collected signals.

Moreover, various threshold-based approaches employ frequency-domain signals, including high- and low-frequency components of HIF voltage and current signals. In (Shahrtash & Sarlak, 2006), the aggregate energy of low-order harmonics serves as the HIF detection criterion. The technique presented in (Keng-Yu et al., 1999) hinges on the energy variance of even harmonics of zero-sequence current at low orders. The HIF detection strategy in (Lima et al., 2018) utilized a short-time Fourier transform (STFT) to isolate the primary harmonic constituents of the phase current, such as the amplitude and phase of the third harmonic, as well as the amplitudes of the second and fifth harmonics. In (Gomes et al., 2018), a HIF detection method proposed leverages fluctuations in high-frequency voltage signals. While these approaches can extract noteworthy HIF features in the frequency domain, the frequency-domain characteristics of nonlinear loads and high-

* Corresponding author.
E-mail address: gaojianhong1994@foxmail.com (J. H. Gao), gmf@fzu.edu.cn (M. F. Guo), S. Lin@hull.ac.uk (S. Lin), dychen@saturn.yzu.edu.tw (D. Y. Chen)

impedance loads exhibit significant similarity, challenging their effective differentiation.

To address the limitation of threshold-based methods using time-domain and frequency-domain signals, more advanced time-frequency analysis methods, empirical wavelet transform (EWT) (Gao et al., 2022), variational mode decomposition (VMD) (Wang et al., 2019; Wang et al., 2022), and Teager-Kaiser energy operator (TKEO) (Biswal et al., 2021), were utilized to achieve HIF detection in the time-frequency domain. With EWT's aid in (Gao et al., 2022), the time-frequency feature component was selected for constructing the permutation variance to detect HIFS. In (Wang et al., 2019; Wang et al., 2022), VMD decomposes zero-sequence currents and extracts useful features for HIF detection. TKEO is computed as a key indicator to distinguish HIF from non-HIF events (Biswal et al., 2021). The underlying principle of these threshold-based techniques involves transforming the original signal from the time domain to either the frequency or time-frequency domain and extracting relevant feature indicators to detect HIFs.

Nevertheless, a major challenge associated with threshold-based methods is the difficulty in establishing an appropriate threshold that adapts to a wide range of fault conditions. Owing to the subtle characteristics of HIFs, determining the optimal threshold presents a critical challenge. Overly high thresholds may fail to identify HIFs, while excessively low thresholds may generate false alarms due to disturbance events.

2) AI techniques are distinct from conventional approaches as they prevent the need for manually defined thresholds. These techniques have been extensively employed in status prognostics and fault diagnosis tasks. Prognostics by AI methods involve developing regression models to predict various aspects such as state-of-health (SOH), remaining useful life (RUL), and future capacity of lithium-ion batteries (Zhang et al., 2021; Zhang et al., 2022; Zhao et al., 2022). In (Zhang et al., 2021), the authors propose a novel hybrid approach combining VMD, particle filter, and Gaussian process regression to predict battery future capacity and RUL. A fusion neural network model, integrating a broad learning system (BLS) and long short-term memory neural network, was developed to predict the capacity and RUL of lithium-ion batteries (Zhao et al., 2022). Particle swarm optimization was utilized to find the optimal global value of BLS in (Zhang et al., 2022). Such integrated methods utilize multiple technologies to achieve the best performance for specified purposes.

As for fault diagnosis in power systems, the typical machine learning methods, such as decision tree (DT) (Samantaray, 2012; Sheng & Rovnyak, 2004), fuzzy interference system (FIS) (Aziz et al., 2012; Zhang et al., 2013), support vector machines (SVM) (Chaitanya et al., 2019), were utilized to address the engineering problems. The DTs in (Sheng & Rovnyak, 2004) were trained by the magnitudes and phases of fault current at the second, third, and fifth harmonics. Then, the proposed technique in (Samantaray, 2012) combined an extended Kalman filter and random forest for effective HIF detection. FLS is a non-linear mapping that includes fuzzy sets, fuzzier, fuzzy rules, an inference engine, and demulsifiers to map inputs to outputs. Adaptive network-based FIS evolved from the FIS to deduce fuzzy rules for HIF detection in (Aziz et al., 2012), while fault identifiers derived from wavelet-transformed transient currents in (Zhang et al., 2013) to accurately identify specified fault types. The method proposed in (Chaitanya et al., 2019) employs VMD-singular value decomposition (SVD) to extract fault-current features and classifies them by SVM. Generally, DT, ANFIS, and SVM were viewed as the traditional AI methods, which have been applied in HIF detection but ever not achieved excellent performance.

With the increasing availability of computational resources, artificial neural networks have become increasingly popular in fault diagnosis and have emerged as a powerful tool for fault detection and classification. For instance, in (Sirojan et al., 2022), the SFFT spectrum was combined with a deep convolutional neural network to detect HIFs. In (Silva et al., 2018), an evolving neural network was used with the discrete wavelet transform to identify electrical current patterns. Similarly, the approach proposed in (Xiao et al., 2022) utilized the 1D variational prototyping encoder and decision tree for feature extraction and fault detection. An improved generative adversarial network was proposed in (Guo et al., 2023) to generate sufficient samples for the HIF detection model. Combining AI techniques with fault diagnosis is essential to fully exploit AI's latent advantages in expression.

While the mainstream methods for HIF diagnosis offer valuable insights, closer examination reveals certain drawbacks. Firstly, for the threshold-based methods, the moment of fault triggering may occur later than the actual fault inception, thus compromising the accuracy of subsequent fault detection. Secondly, previous research only utilized short-period data, from which various features were extracted to enable further detection. However, this approach fails to capture the more general characteristics of HIF, such as distortion and randomness, on a longer timescale. We propose a HIF diagnosis approach for fault triggering and detection to overcome these limitations. Specifically, our approach aims to rapidly filter suspected fault events from massive real-time events and determine the moment of fault inception for fault triggering. Subsequently, fault detection methods are employed to accurately classify the suspected fault events.

Following the proposed paradigm, a semantic-segmentation-based approach is proposed using the signal envelope (SE) and Hilbert marginal spectrum (HMS) to realize real-time HIF diagnosis. The main contributions of this paper are summarized as follows:

1) *Fault Triggering Aspect:* This paper integrates the concept of semantic segmentation in HIF diagnosis for the first time. The proposed approach uses zero-sequence voltage as input. It implements pixel-wise prediction through 1D-UNet to realize fault triggering, locate the transient process of the suspected fault events, and determine the moment of fault inception.

2) *Fault Detection Aspect:* The Hilbert-Huang transform (HHT) is applied to zero-sequence voltage to obtain both the SE and HMS, which are representative of the distortion and

randomness of HIF over a long timescale, respectively. These features are then converted into images, and the ResNet18 is utilized to judge the HIF based on distortion and randomness characteristics.

3) *Diagnosis Framework and Deployment Aspect*: An industrial prototype is constructed by proposing and deploying a real-time HIF diagnosis framework on the NVIDIA Jetson TX2. The proposed approach is validated under the 10 kV test system, and the results show that it can achieve excellent accuracy and efficiency, indicating considerable potential for future industrial applications.

This paper is organized as follows: Section 2 analyzes the characteristics of HIF, while Section 3 details the basic theories of the proposed approach. Section 4 discusses relevant test results, and Section 5 provides the main conclusions.

2. Characteristics analysis of HIF

In a 10kV resonant distribution network, a HIF is a unique type of single-phase-to-ground fault (SPGF) that can occur in an overhead line. When the overhead line comes into contact with high-impedance media such as branches, gravel, concrete, and asphalt pavement, it is susceptible to creating an arc, resulting in a HIF. The fault resistance range of HIF can reach several hundred or even thousands of ohms, causing the fault current to be weak and nonlinear, with random variations (Wei et al., 2021).

Diagnosing HIF remains a challenging task for existing methods. As the available field recordings of HIF are limited and insufficient, a 10 kV full-scale test system was built to simulate HIFs under various scenarios to analyze and verify the performance of the proposed approach. The topology of the 10 kV full-scale test system and the diverse materials used, such as branches, grass, gravel, and an arc in the cable, are shown in Fig. 1.

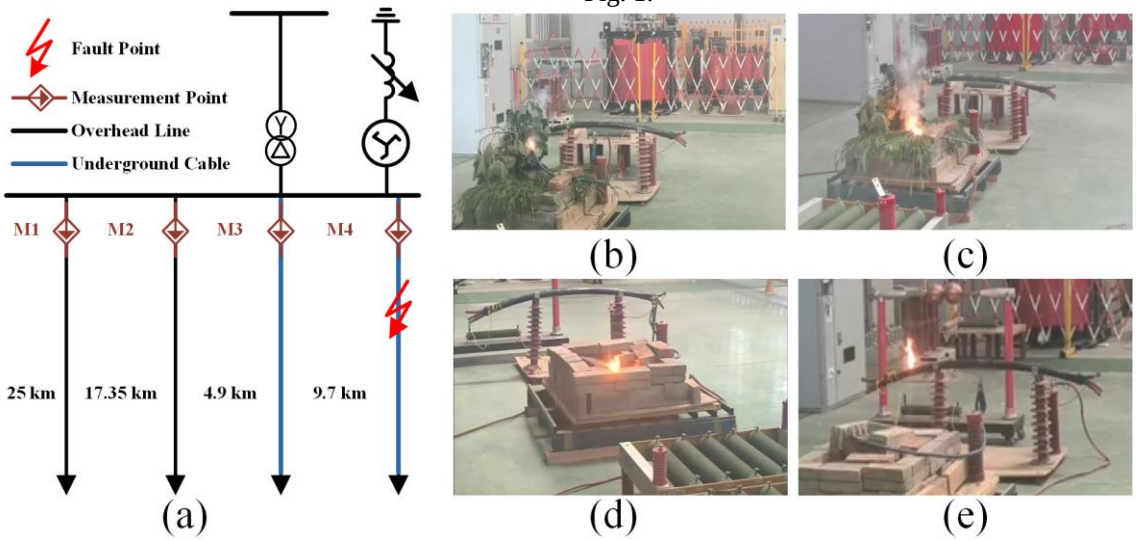

Fig. 1. 10 kV full-scale test system. (a)Topology. (b) Branches. (c) Grass. (d) Gravel. (e) Arc in the cable.

In previous literature, the main characteristics of HIF, including distortion, randomness, and intermittence, have been highlighted (Wei et al., 2021). These characteristics are most pronounced in fault currents. Therefore, the zero-sequence current at the measurement point is usually captured to represent the fault current, which cannot be directly measured. However, it should be noted that as the distance between the measurement point and the fault point increases, the features of HIFs on the zero-sequence current become less clear and observable. With increasing distance, the capacitive grounding current gradually increases, potentially submerging the weak-amplitude fault current since the zero-sequence current at each measurement point on the fault feeder comprises both the capacitive grounding and fault currents.

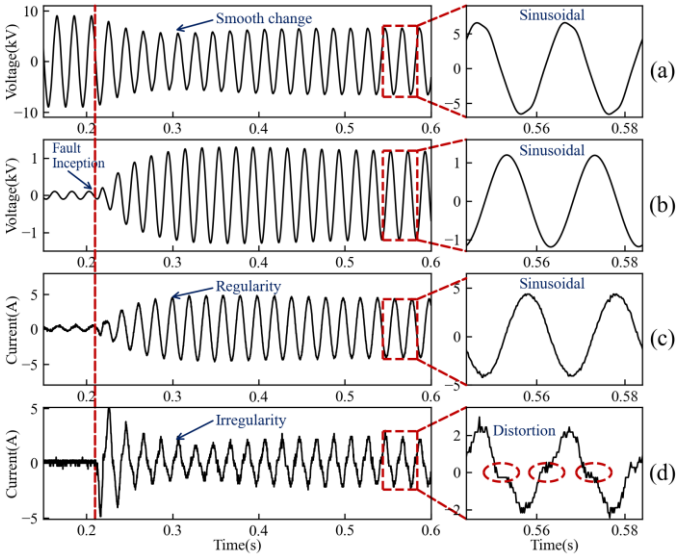

Fig. 2. HIF via gravel implemented by 10 kV full-scale test system. (a) Fault phase voltage. (b) Fault zero-sequence voltage. (c) Fault zero-sequence current of the measurement point. (d)

Fault current of fault point.

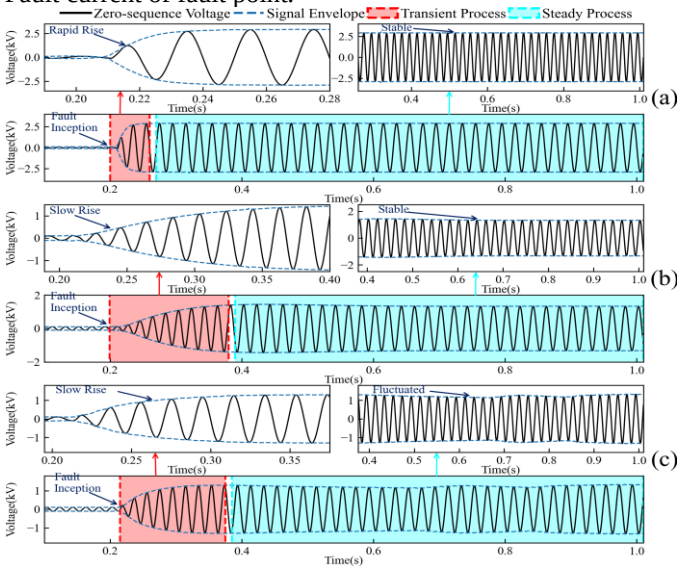

Fig. 3. Whole waveform and its transient and steady process. (a) SPGF via low fault resistance at 200 ohms. (b) SPGF via high fault resistance at 3k ohms. (c) HIF via gravel.

To support this intuition, we present field fault waveforms in Fig. 2. During the steady phase of a HIF, the fault zero-sequence voltage experiences a slow increase in amplitude. Following this, the waveforms of the fault zero-sequence voltage and current at the measurement point become sinusoidal and exhibit a linear relationship. Notably, the zero-sequence current at the head-end does not show any irregularities, suggesting that the irregularities of the fault current may be substantially masked at the substation outlet or measurement point far from the fault point. As a result, HIF diagnosis methods using zero-sequence current may fail, depending on the distance between the fault point and measurement points.

To address this issue, we chose zero-sequence voltage as the research objective for finding a useful feature to realize HIF diagnosis in real time. Two SPGFs with low fault resistance at 200 ohms and high fault resistance at 3k ohms were conducted in the 10 kV full-scale test system. It is essential to note that there is a significant difference between HIF and SPGF with high fault resistance, where the former is accompanied by intermittent arcing, and the latter is typically used to verify methods through a fixed fault resistance. The waveforms of the whole zero-sequence and the transient and steady processes of the three faults are shown in Fig. 3.

Various faults' transient and steady processes deserve attention, as shown in Fig. 3. During the transient process, the SPGF with low fault resistance had the shortest duration and showed a rapid rising tendency. In contrast, HIF and SPGF with high fault resistance were longer and consistently tended to rise slowly. In the steady process, the zero-sequence voltage of the SPGFs with fixed resistance was regular and stable. On the contrary, the waveform of HIF through gravel exhibited random characteristics due to the nonlinearity and time-varying impedance. It can be inferred that the actual HIF differs from the other two ideal SPGFs with fixed fault resistance, depending on whether the random characteristics are generated by intermittent arc. Therefore, long-term data is required to represent the random characteristics of HIF and distinguish it from other events.

Based on the above comparison between HIF and SPGF with a fixed resistance, it can be seen that zero-sequence voltage with a large timescale can be exploited to observe the random characteristics of HIF during the steady process. However, this analysis, based on a time-domain signal, does not fully describe the characteristics of HIF in the frequency domain. Therefore, a time-frequency analysis was conducted in Section 3, which, along with the results documented in Section 3 and Section 4, confirms the validity of adopting zero-sequence voltage for HIF diagnosis.

3. Proposed HIF diagnosis approach

A novel approach for HIF diagnosis was presented, consisting of two stages: fault triggering and fault detection. This paper, the 1D-UNet model is used for one-dimensional data to determine the transient process (TP) of suspected fault events and the moment of fault inception. The long-term zero-sequence voltage of the suspected fault events is then processed through feature extraction and detection using the ResNet18 model to detect a HIF. Specifically, the SE and HMS are extracted using HHT, representing distortion and randomness, respectively. These features are transformed into images and used as input to a ResNet18 model to implement fault detection. The type of suspected fault events is confirmed through a final comprehensive judgment. If the long-term waveform of the suspected fault event exhibits both distortion and randomness characteristics simultaneously, such event is identified as a HIF.

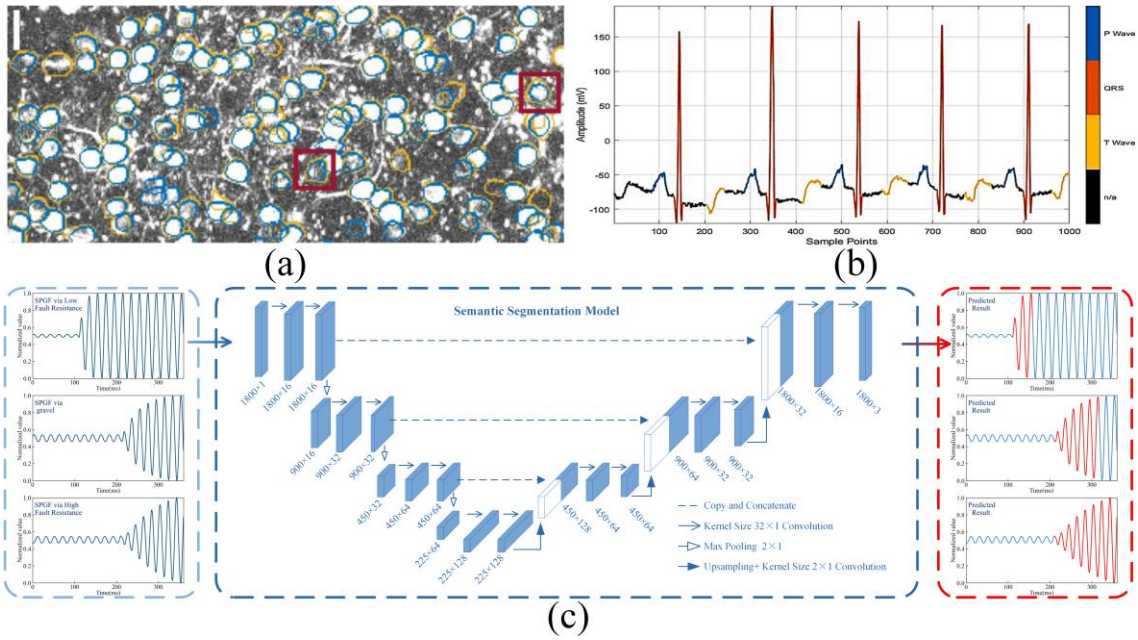

Fig. 4. Application of semantic segmentation (a) Neuron segmentation (Bao et al., 2021). (b) ECG wave interpretation (Londhe & Atulkar, 2021). (c) Fault triggering in the proposed approach.

3.1. Fault triggering

In this paper, distinguishing fault inception is a prerequisite for subsequent fault detection. Achieving a balance between sensitivity and reliability is crucial for the triggering methods. Typically, triggering methods with high sensitivity exhibit low reliability. Methods with sensitive thresholds are susceptible to maloperation when disturbance events occur. On the other hand, actual HIF may not trigger methods with high thresholds due to its faint fault characteristic in certain extreme conditions. More generally, the uncontrolled delay of the fault moment judged by threshold-based methods can compromise the robustness and effectiveness of subsequent fault detection.

Semantic segmentation techniques have found extensive applications in various domains, particularly in the medical analysis (Mo et al., 2022), where they divide a given image or sequence into visually meaningful regions for further analysis and comprehension (Wang et al., 2010). Fig. 4 (a) and (b) showcase two different applications of semantic segmentation, respectively. In (Bao et al., 2021), a visual representation of active neuron segmentation is presented, which assists in understanding the functions of an animal's brain. Meanwhile, (Londhe & Atulkar, 2021) showcases a continuous electrocardiogram (ECG) wave segmentation example, in which distinct colors for easy interpretation denote regions containing specific medical information. Motivated by these applications, we propose integrating semantic segmentation techniques in HIF diagnosis and identifying a significant gap in their application in power systems. In (Yuan & Jiao, 2022), the authors employed a fully convolutional network to detect fault feeders, converting waveform detection into the task of image segmentation. However, the use of semantic segmentation models in power systems, particularly in HIF diagnosis, remains unexplored.

As shown in Fig. 4(c), we introduce a novel fault-triggering method that uses 1D-UNet to extract semantic information from the zero-sequence voltage. The primary objective of the proposed 1D-UNet is to detect the transient process (TP) of suspected fault events and determine the inception moment. In real-time tasks, the smallest disposition unit is the sliding time window with a fixed length divided into smaller segments representing different events. The measured signals, such as zero-sequence voltage, are inherently heterogeneous, often containing a combination of segments, conditions, and sequence patterns (Oh et al., 2019).

Upon inputting the original data into the 1D-UNet, the TP of the suspected fault event is inferred. The 1D-UNet makes a class prediction at every sampling point, with two classes -'TP' and 'N/A'- to be predicted for each point. The 'TP' class indicates the transient process of the suspected fault event, which is depicted in red in the output waveforms. The 'N/A' class, marked in blue, signifies a sampling point associated with the background instead of the previous class. Sampling points assigned to 'N/A' share the same color as the original signal. Consequently, the inception moment of the suspected fault event is determined by the output of the 1D-UNet.

3.2. Fault detection

After determining fault inception, an effective method for fault detection is needed to confirm the type of suspected fault events, focusing on distinguishing HIF from other events. Fault detection comprises two exact steps: feature extraction and detection.

1) *Feature extraction*

In the feature extraction process, the raw signal is transformed into distinctive properties that can be utilized in fault detection. The SE and HMS of the zero-sequence voltage are extracted by using HHT. These two features represent the

distortion and randomness characteristics of HIF, respectively. The theoretical basis of SE and HMS is as follows.

SE is a time-domain analysis method that measures the amplitude of the signal envelope over time. It can detect changes in the signal's amplitude caused by the HIF fault. The equation for calculating SE can be expressed as:

$$SE(t) = \sqrt{[x^2(t) - m_x^2(t)]^2 + [y^2(t) - m_y^2(t)]^2} \quad (1)$$

Where $x(t)$ and $y(t)$ are the real and imaginary parts of the analytic signal, respectively, and $m_x(t)$ and $m_y(t)$ are their corresponding moving averages.

The theoretical basis of SE lies in the Hilbert transform, a mathematical tool used to analyze signal processing in communication systems. Essentially, the SE is obtained from the signal's Hilbert transform, leading to the extraction of the envelope.

On the other hand, HMS is a frequency-domain analysis method that measures the marginal spectrum of a signal, which is defined as:

$$HMS(f) = \frac{1}{T}\int_0^T |x(t)\, f(t)|^2 \, dt \quad (2)$$

Where T is the signal's time duration, $x(t)$ is the signal, and $f(t)$ is a frequency-modulated function that varies between 0 and 1.

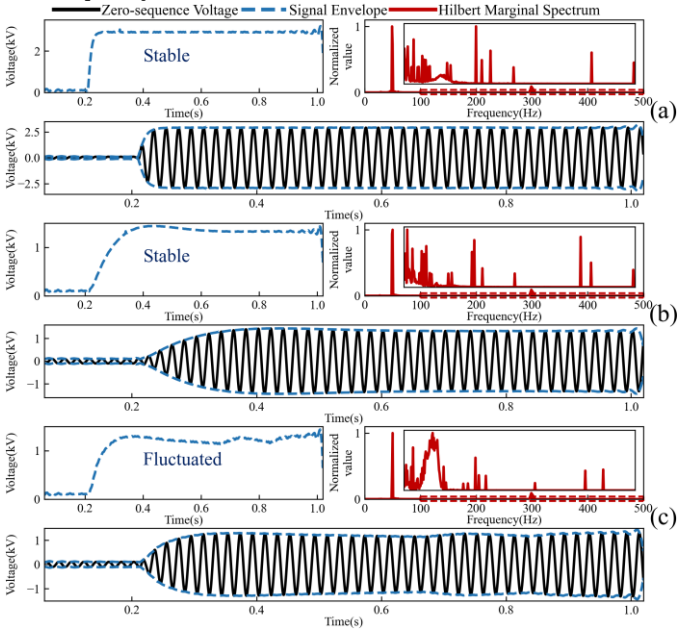

Fig. 5. Whole waveform and its SE and HMS. (a) SPGF via low fault resistance at 200 ohms. (b) SPGF via high fault resistance at 3k ohms. (c) HIF via gravel.

Figure 5 depicts the zero-sequence voltage with its SE and HMS for different fault types. The SEs obtained from fault events exhibit distinct characteristics. For SPGF, the SE remains stable after fault inception, whereas the SE of HIF fluctuates irregularly. As the base frequency component of 50Hz has the highest proportion, it can obscure the information of other characteristic frequency components in the full frequency range. Therefore, we mainly focus on the magnified subfigure in Fig. 5, which shows the HMS from 100Hz to 500Hz. The main frequency distribution range of the signal and the marginal spectrum peak value at the same frequency exhibit significant differences among the HMS. Since the HMS is obtained by integrating the Hilbert spectrum along the time axis, it provides the total energy distribution of frequency to represent distortion characteristics. Therefore, these two features are key to distinguishing different fault events in this paper. We converted SE and HMS into grayscale images to facilitate fault detection and used the following ResNet18 model.

2) *Detection*

To carry out fault detection, we employed a ResNet18 classifier, a commonly used deep neural network for image recognition tasks, due to its residual learning structure that can help mitigate the problems of vanishing and exploding gradients (He et al., 2016). To identify the unique characteristics of the SE and HMS images of the diverse fault samples, we chose to use ResNet18 in this study. Fig. 6 illustrates the structure of ResNet18. This model takes a pair of grayscale images representing the SE and HMS as input. It then assigns one of four labels – 'Distortion', 'Non-Distortion', 'Randomness', or 'Non-Randomness' – to characterize the input images, which helps classify suspected fault events.

3.3. Integrated HIF diagnosis flowchart

The integrated HIF diagnosis flowchart is presented in Fig. 7, and the detailed steps are described as follows:

Step 1. Real-time Data Recording: Real-time monitoring of the zero-sequence voltage is performed using a sliding window with a window length and slide size of 18 power frequency cycles (PFCs) and one PFC, respectively. As the sampling rate is set to 5 kHz, the corresponding window length and slide sizes are 1800 and 100 sampling points, respectively.

Step 2. Fault Triggering: For the real-time data of each sliding window, the 1D-UNet is used to obtain pixel-wise prediction results to identify the moment of fault inception. Based on these results, the transient process (TP) of the suspected fault events is distinguished to determine the moment of fault inception. The post-fault data in a longer timescale is then obtained for fault detection, with the length of the post-fault data set to 50 PFCs, or 5000 sampling points.

Step 3. Fault Detection: The zero-sequence voltage is processed using HHT to obtain the SE and HMS, which are then converted into grey-scale images for ResNet18 analysis. ResNet18 provides four possible prediction results, including Distortion & Randomness (DR), Distortion & Non-Randomness (DNR), Non-Distortion & Randomness (NDR), and Non-Distortion & Non-Randomness (NDNR), as shown in Fig. 7.

Step 4. Final Judgment: Based on the ResNet18 results and depicted in Fig. 7, the final judgment follows this principle: HIFs are confirmed if the outcome is DR. If any of the other three combinations arise, the system evaluates data from the next sliding window.

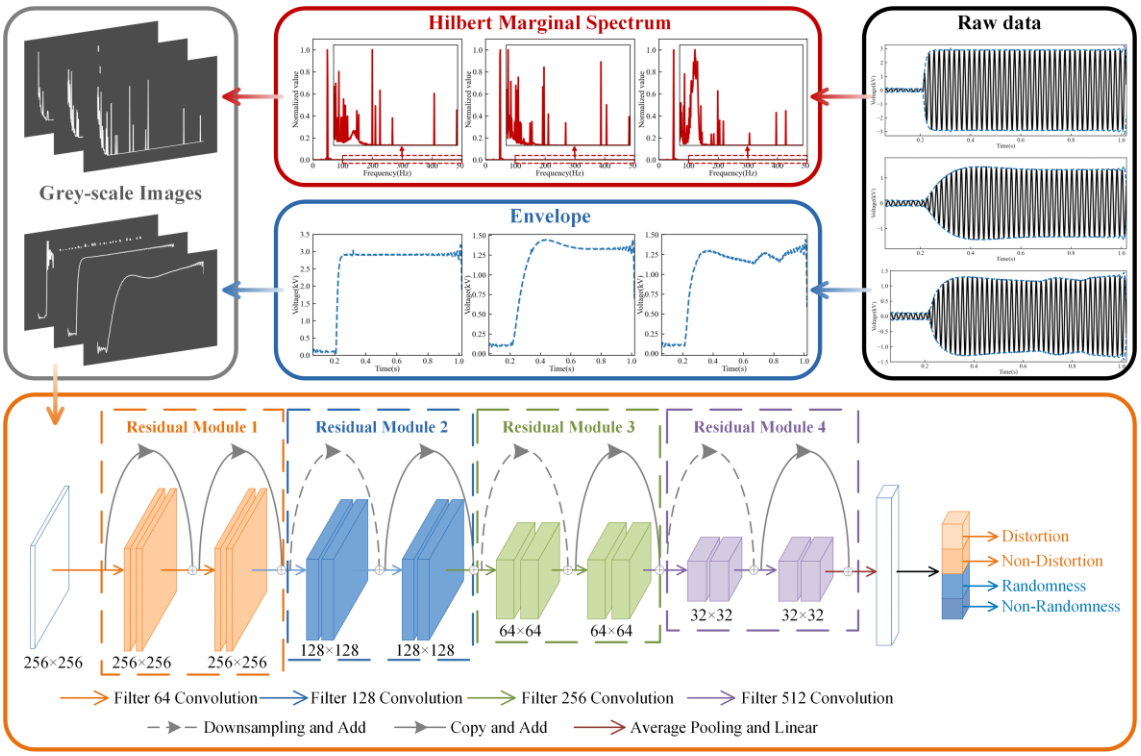

Fig. 6. Architecture of ResNet18.

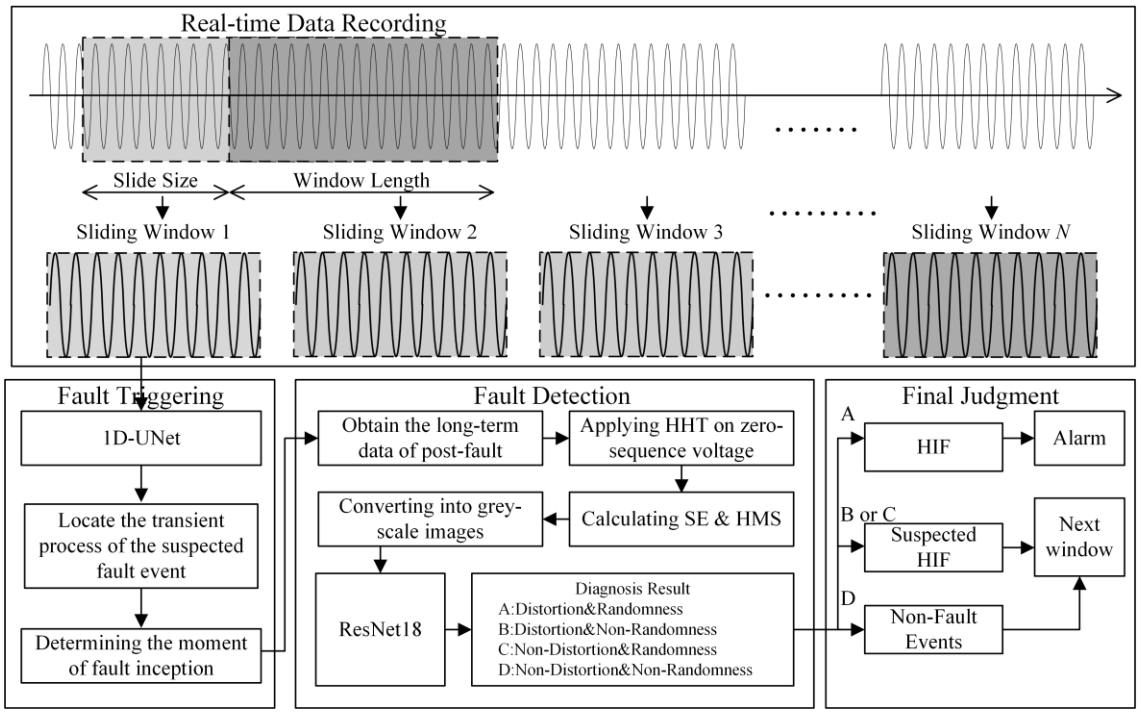

Fig. 7. Integrated HIF diagnosis flowchart

4. Case study

As illustrated in Fig.8, we used the PSCAD/EMTDC platform to construct a 10 kV resonant distribution networks simulation model to generate sufficient simulation events to build the dataset. The Emanuel model was employed in the model to simulate the half-cycle asymmetry of the HIF current through two resistances, Rn and Rp, with varying resistance values. Additionally, two antiparallel DC sources V*n* and V*p*, connected through two diodes D*n* and D*p*, were incorporated to control the intermittent reignition and extinction of the fault current in proximity to the zero-crossing point. The detailed parameters of the 10 kV distribution network simulation model can be found in the literature (Xiao et al., 2022).

While simulation models can only approximate the distortion characteristics of HIFs to some extent and not their random characteristics, the testing data collected from the 10 kV test

system in Fig. 1 were also utilized to develop the training and testing datasets for the 1D-UNet and ResNet18 models. Table 1 presents detailed information on the samples from the 10 kV test system and simulation models to clarify the dataset's distribution.

The annotation requirements for the 1D-UNet and ResNet18 models are distinct. The ResNet18 model utilizes image-level annotations, which is typical in image recognition tasks. However, the 1D-UNet model requires numerous pixel-level annotations, which can be time-consuming and challenging. The absence of readily available annotation tools for electrical signals further compounds this challenge. We developed a new annotation tool called "LabelSIG," specifically adapted for electrical signals to address this gap.

Table 1
Dataset distribution

Data Source	Event Type	Description	Number
Simulation model	HIF	Cement, Dry grass, Wet grass	100
	SPGF	Fault resistance(kΩ): 0.2, 2, 3	100
10 kV full-scale test system	HIF	Branches, Grass, Gravel, and Arc in the cable	84
	SPGF	Fault resistance(kΩ): 0.2,0.5,1,2,3 Fault initial angle(°): 0,30,60,90	50

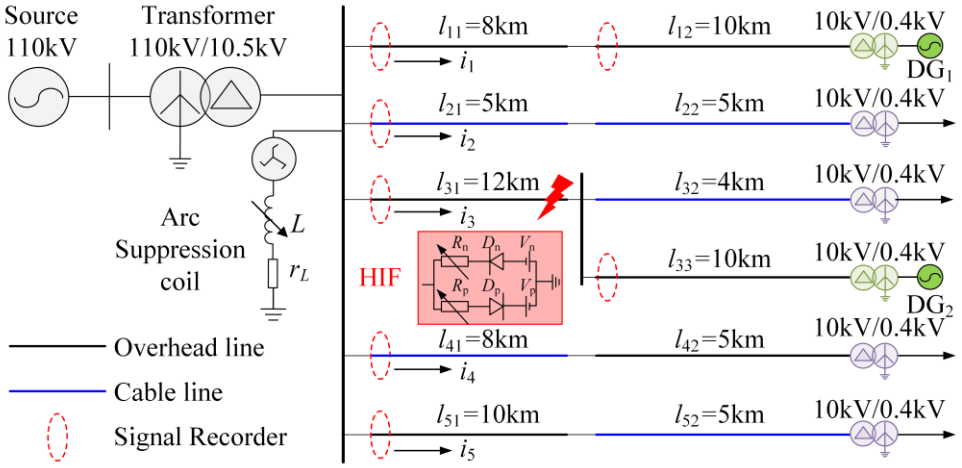

Fig. 8. Simulation model of 10 kV resonant distribution network

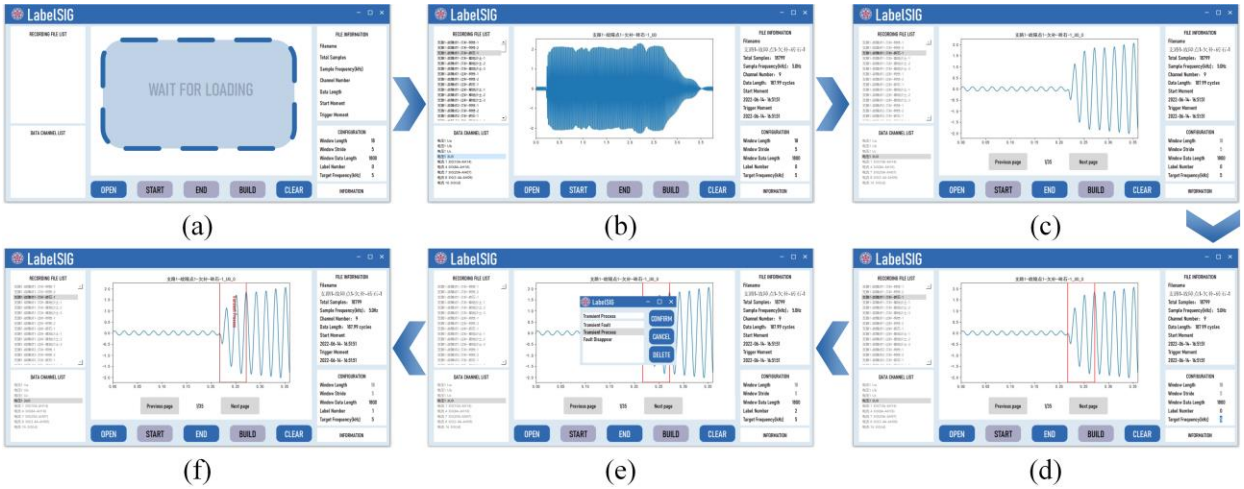

Fig. 9. Annotation procedure of LabelSIG. (a) User interface. (b) Upload data set. (c) Obtain multiple subsequences. (d) Create annotation region. (e) Select the annotation label. (f) Visualized annotation result.

Figure 9 showcases LabelSIG, a Python-based electrical signal labeling tool that utilizes Qt for its graphical interface. It can directly extract information from Common Format for Transient Data Exchange (COMTRADE) records, a standard file format. The annotation procedures of LabelSig are illustrated in Fig.9, where the datasets are uploaded first, and multiple subsequences are automatically generated by the tool, as shown in Fig.9 (b)-(c). The user can then observe each subsequence and perform semantic annotation, which involves creating an annotation region and selecting a suitable label from the list. These operations and the visualized annotation result are presented in Fig.9 (d)-(f).

4.1. Implementation and evaluation

The datasets were split into 70% for training and 30% for testing the proposed models. The computer used for training has

a 3.2 GHz Intel® Core™ i7-8700, 16.00 GB RAM, and NVIDIA® GeForce RTX-1060. The Pytorch framework was used for training and testing, with specific hyperparameters shown in Table 2. Selecting the right hyperparameters is crucial for optimal model performance, as they are set before training and not learned during the process. In our proposed approach, we used a trial-and-error method to determine the hyperparameters that yielded the best performance on the dataset in the proposed approach. The hyperparameters presented in Table 2 were chosen through this process to attain the best performance for our proposed approach.

Table 2

Hyperparameter of two models

Hyperparameter	1D-UNet	ResNet18
Learning rate	0.001	0.005
Training epoch	50	60
Optimizer	Adam	Adam
Batch Size	10	4

Since the proposed approach consists of two distinct stages with differing model designs, we will present a detailed evaluation of each model below.

1) *Fault Triggering Evaluation:* The proposed 1D-UNet tended to generalize well from the training data without requiring additional network regulation. The early stopping strategy was utilized to prevent overfitting, and the 1D-UNet was trained for only 50 epochs. The testing accuracy of the model reached 0.96, as shown in the accuracy and loss curves in Fig. 10. The confusion matrix in Fig.10(c) demonstrates that the semantic segmentation model can accurately identify the transient process (TP) of suspected fault cases.

To offer a clearer evaluation of the semantic segmentation model's performance, we showcase three zero-sequence voltage signals and their associated activation maps in Figure 11. These signals represent HIF, SPGF with low fault resistance, and SPGF with high fault resistance. Each color on the color bar in Fig.11 corresponds to a specific class, with the predicted results appearing lighter than the annotated labels. Additionally, we measure the accuracy of fault triggering performed by the 1D-UNet using the triggering deviation, which is the distance between the actual and predicted moments of fault inception. In Fig.11, a positive value indicates that the predicted moment is later than the actual moment. In contrast, a negative value indicates that the predicted moment is earlier than the actual moment.

In light of the primary objective of fault triggering in this investigation, which entails identifying the TP of zero-sequence voltage after the occurrence of a HIF, it is rational to postulate that precise labeling of individual sampling points would substantially improve this procedure. This granular labeling approach resembles pixel classification-centric image semantic segmentation tasks, for which the UNet architecture was expressly devised. The encoder-decoder structure of the UNet model enables the discernment of local and global features, culminating in outstanding classification performance. This proficiency extends to the examination of 1D sequential data as well.

These insights prompted the conception of the 1D-UNet for fault triggering, wherein the initial sample point of TP is considered as the fault moment, which aids in subsequent fault detection. Although the trained 1D-UNet demonstrates high accuracy in classifying most sampling points, the fault-triggering precision remains contingent upon its performance. Consequently, future research endeavors should concentrate on augmenting the tolerance performance of the proposed approach.

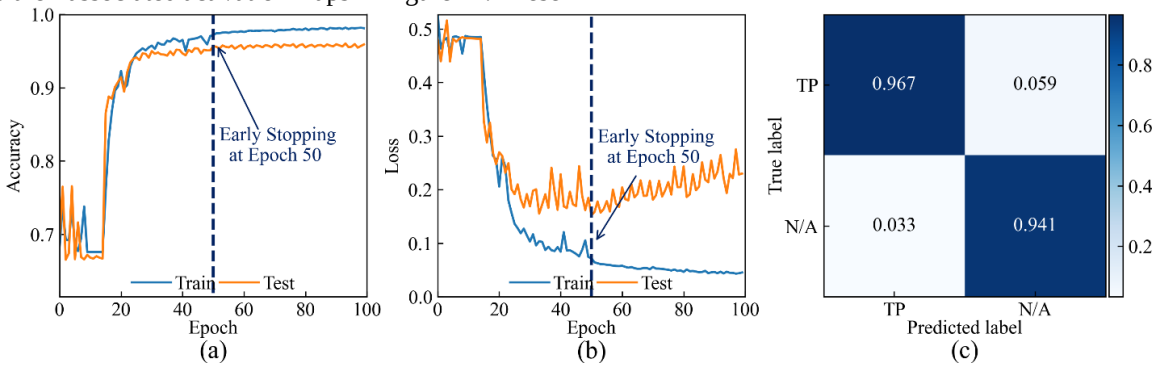

Fig. 10. Visualization of the 1D-UNet training process.
(a) Accuracy curve. (b) Loss curve. (c) Confusion matrix

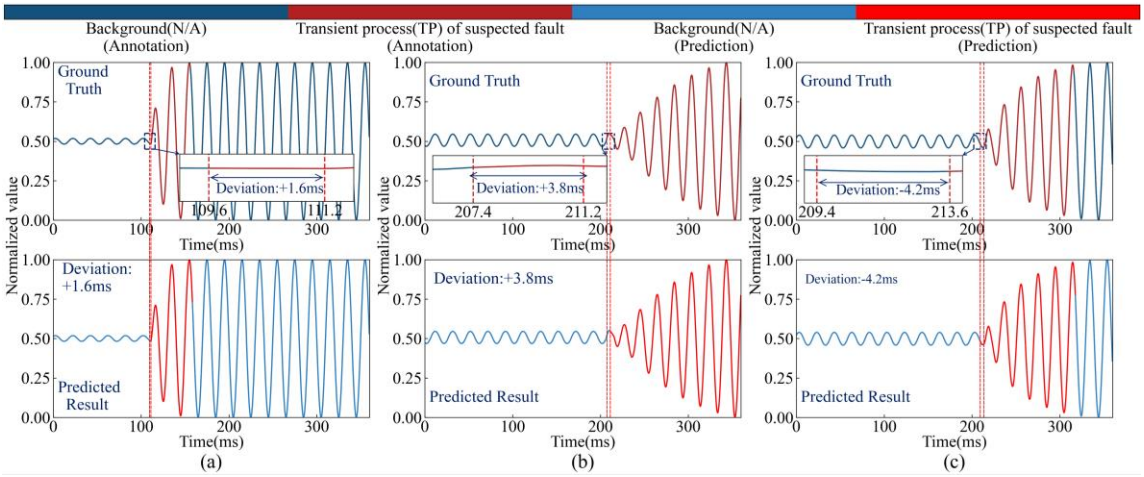

Fig. 11. Semantic segmentation of zero-sequence voltage under diverse scenarios. (a) SPGF via low fault resistance at 200 ohms. (b) SPGF via high fault resistance at 3k ohms. (c) HIF via gravel.

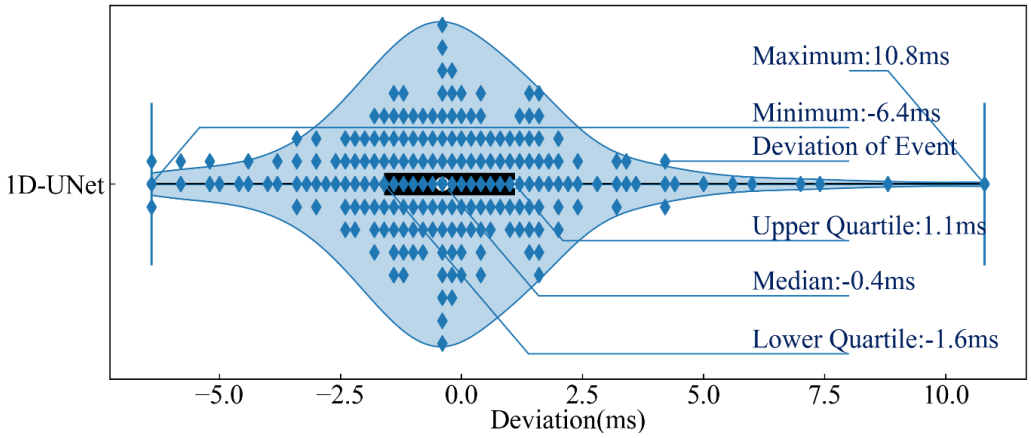

Fig. 12. Triggering deviation of the 1D-UNet

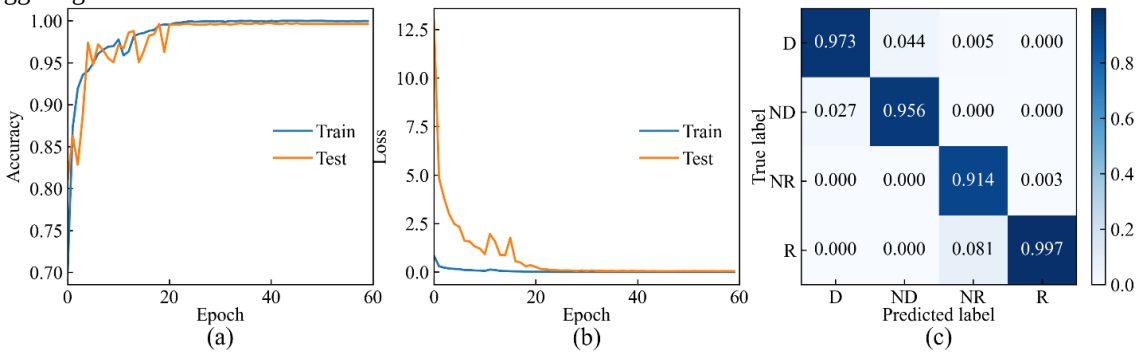

Fig. 13. Visualization of the ResNet18 training process.
(a) Accuracy curve. (b) Loss curve. (c) Confusion matrix.

In Fig.12, the distribution of triggering deviation in the test sets is depicted using a violin plot, where the diamond marker denotes the triggering deviation of each event in the test sets. The median of the triggering deviation is -0.4 ms, while the maximum positive and negative deviations are 10.8 ms and -6.4 ms, respectively. The proportion of cases with extreme deviation is small, typically one or two cases, primarily located at both ends of the violin plot. Most triggering deviation values are concentrated around 0 ms, indicating that the proposed 1D-UNet model can accurately predict the moment of fault inception in most cases.

2) *Fault Detection Evaluation:* Upon obtaining the grey-scale images of SE and HMS, the detection of HIF was performed using ResNet18. The training process and performance evaluation of the ResNet18 model are presented in Fig.13, which includes the accuracy curve, loss curve, and confusion matrix. In the confusion matrix, the abbreviations 'D', 'ND', 'NR', and 'R' correspond to 'Distortion', 'Non-Distortion', 'Non-Randomness', and 'Randomness', respectively. The detection results demonstrated that the ResNet18 achieved a high accuracy rate of 0.97 on the test sets after 20 training epochs. The confusion matrix (Fig. 13(c)) indicates that the output of the ResNet18 model matched the corresponding

ground truth. Based on the ResNet18 output, the type of suspected fault event was determined.

In addressing the fault detection facet of the proposed approach, this study employs SE and HMS to capture the randomness and distortion inherent in HIF over extended durations. Despite the limited literature on the application of long-scale signals for HIF identification, this work represents the first instance of harnessing macro-scale zero-sequence voltage data to reveal HIF's unique nonlinear and unstable characteristics. The scarcity of documented actual fault events over prolonged periods necessitates further validation by the proposed developed prototype applied in real distribution networks to obtain sufficient macro-scale zero-sequence voltage data. Sustained research and experimentation in this domain will contribute to refining and optimizing the model's performance, ultimately ensuring its effectiveness and reliability in practical applications.

3) *Comprehensive Evaluation:* To evaluate the computation complexity of the proposed approach comprising 1D-UNet and ResNet18, we utilized several indicators presented in Table 3 to assess the method's space and time complexity.

The floating point operations per second (FLOPs) for 1D-UNet and ResNet18 are 1.35 G and 35.71 G, respectively. The model size of 1D-UNet is 18.25 MB, while the model size of ResNet18 is 42.61 MB. Regarding trainable parameters, 1D-UNet has 1.58 million, while ResNet18 has 42.61 million. Furthermore, the total training time for 1D-UNet is 16 minutes, whereas, for ResNet18, it takes 66 minutes. The inference time for 1D-UNet is 15.78 ms, and for ResNet18, it is 49.16 ms. This analysis demonstrates that the proposed approach, which combines 1D-UNet and ResNet18, exhibits reasonable computation complexity while maintaining high performance in diagnosing HIF for resonant distribution networks. Despite the reasonable computation complexity, the proposed method maintains high performance in fault diagnosis for resonant distribution networks. Importantly, the proposed approach can be deployed in AI hardware platforms, such as TX2, as mentioned in Section 4.3, and can meet the requirements for engineering applications. This adaptability ensures that our approach is practical and effective in real-world scenarios.

Table 3
Computation complexity of two models

Computation Indicator	1D-UNet	ResNet18
FLOPs	1.35 G	35.71 G
Model Size	18.25 MB	42.61 MB
Trainable Parameters	1.58 M	42.61 M
Training Time	16 min	66 min
Inference Time	15.78 ms	49.16 ms

Environmental noise can distort fault signals, and there is no worldwide consensus on the signal-to-noise ratio (SNR) for zero-sequence voltage in distribution networks. Different countries follow their guidelines, but some international organizations, such as IEEE Standard ("IEEE Standard for Interconnection and Interoperability of Distributed Energy Resources with Associated Electric Power Systems Interfaces," 2018), require that the SNR of zero-sequence voltage signals in power systems connected to distributed energy resources should not be less than 20 dB. To assess the anti-interference performance of the proposed method, Gaussian white noise (with SNRs of 20 dB, 25 dB, 30 dB, and 35 dB) is added to the zero-sequence voltage signals. Table 4 indicates that the accuracy performance of 1D-UNet and ResNet18 is affected by noise interference, with higher noise levels causing a decrease in accuracy for both models. However, the testing results in Table 4 show that both models can still achieve an accuracy exceeding 0.9 even with 20 dB noise interference.

Table 4
Accuracy of noise interference for two models

SNR (dB)	Accuracy	
	1D-UNet	ResNet18
20	0.9285	0.9045
25	0.9442	0.9111
30	0.9498	0.9497
35	0.9522	0.9545

To mitigate the inherent bias associated with employing a single testing dataset, we implemented a K-fold cross-validation method, setting K to 4, for partitioning the comprehensive dataset, which encompasses both training and testing datasets. The dataset was systematically divided into three subsets designated for training and one for testing, with a cyclical rotation of the training and testing sets. The other hyperparameters utilized in the model training process were maintained following the specifications delineated in Section 4.1. The outcomes of the K-fold cross-validation for the proposed methodology are illustrated in Fig. 14 and Fig. 15.

As depicted in Fig. 14 and Fig. 15, the cross-validation results revealed that the two models, specifically designed for fault triggering and fault detection, exhibited outstanding performance. Notably, the 1D-UNet achieved an accuracy surpassing 0.95 and loss values below 0.2, while the ResNet18 attained accuracy exceeding 0.96 and loss values under 0.05. Consequently, the proposed approach, integrating 1D-UNet and ResNet18, demonstrates exceptional generalization capabilities and robustness, rendering it suitable for subsequent engineering applications.

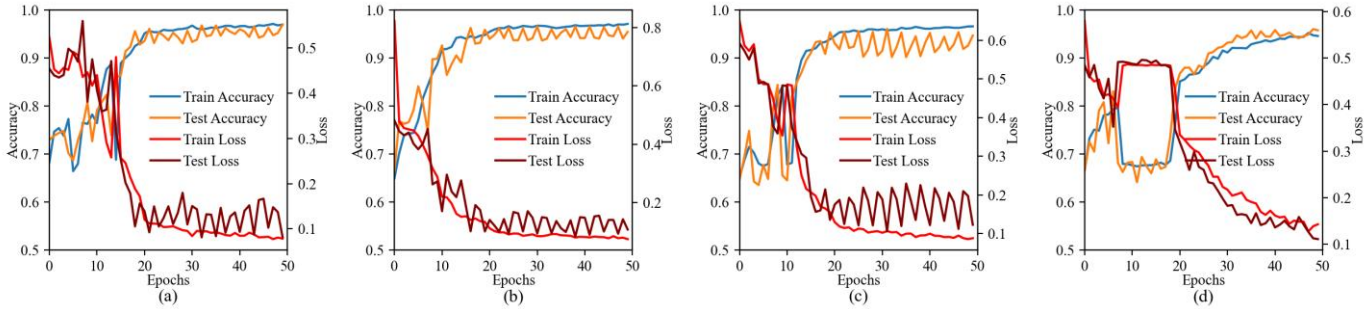

Fig.14. K-fold cross-validation of 1D-UNet
(a) Fold 1 . (b) Fold 2. (c) Fold 3. (d) Fold 4.

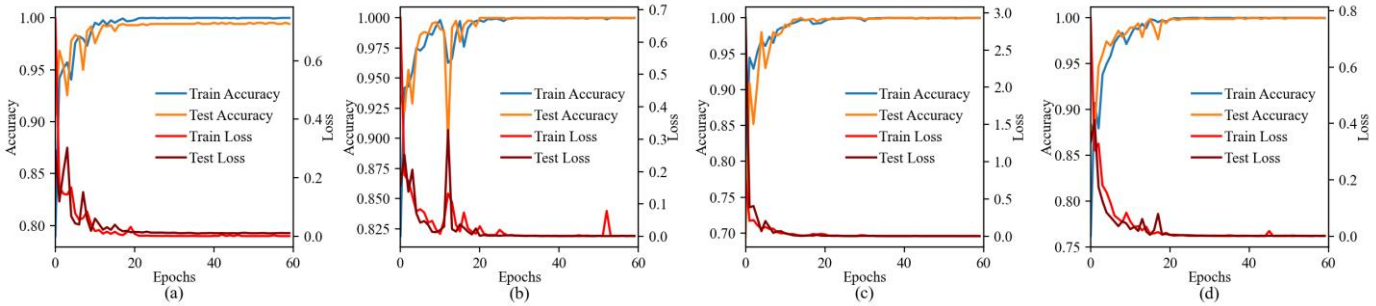

Fig.15. K-fold cross-validation of ResNet18
(a) Fold 1. (b) Fold 2. (c) Fold 3. (d) Fold 4.

In the field of AI models, accuracy is widely recognized as the primary statistical indicator for performance evaluation. However, when dealing with class-imbalanced datasets that exhibit a significant disparity between positive and negative labels, accuracy alone cannot fully assess the model's performance. To overcome this limitation, two other statistical indicators, Precision and Recall, are introduced in equation (3) and equation (4) to assess the performance of the proposed approach.

$$Precision = \frac{TP}{TP + FP} \tag{3}$$

$$Recall = \frac{TP}{TP + FN} \tag{4}$$

Where TP means true positives, which are positive cases correctly identified, FP refers to false positives, where negative cases are wrongly labeled as positive. TN stands for true negatives, which are negative cases predicted accurately. Finally, FN represents false negatives, where positive cases are incorrectly classified as negative.

In large-scale datasets, precision and recall often restrict each other, making it challenging to accurately evaluate the model's overall performance. Therefore, the equation (5) introduces the F-score, an indicator that considers both precision and recall, to reflect the performance of the proposed approach.

$$F_\beta = \left(1 + \beta^2\right) \cdot \frac{Precision \cdot Recall}{Precision + Recall} \tag{5}$$

Where β is chosen as one such that recall is considered important as precision, F_1-score is adopted as in this paper.

Table 5 reveals that both models exhibit strong performance across all the statistical indicators. Specifically, the 1D-UNet model achieves an Accuracy of 0.9586, Precision of 0.9585, Recall of 0.9586, and an F_1-score of 0.9585. On the other hand, the ResNet18 model demonstrates slightly better results with an Accuracy of 0.9645, precision of 0.9659, recall of 0.9645, and an F_1-score of 0.9647.

Table 5
Statistical methods of two models

Statistical Indicators	1D-UNet	ResNet18
Accuracy	0.9586	0.9645
Precision	0.9585	0.9659
Recall	0.9586	0.9645
F_1-score	0.9585	0.9647

4.2. Comparison to existing approaches

To evaluate the performance of the proposed approach at each stage, we compare it with other methods on a stage-by-stage basis.

1) *Fault Triggering Stage*: Most protective devices use threshold-based methods that rely on the zero-sequence voltage threshold to detect fault inception, denoted as Method A in this study, with a threshold set to 15% of normal phase voltage. The method proposed in the literature (Lin et al., 2019) was also implemented as Triggering Method B to achieve fault triggering using wavelet transform. It was compared with Triggering Method A and the proposed fault-triggering approach. In most fault-triggering methods, the time required for real-time detection deserves more attention. Therefore, the comparison results of triggering deviation and time consumption are presented in Fig. 16 and Table 6, respectively, indicating that the 1D-UNet can capture the fault inception and achieve superior performance by a large margin. In contrast, Triggering Method A, based on a fixed threshold, cannot accurately locate the moment in high-impedance faults with low amplitudes, despite having the shortest time consumption.

Triggering Method B adopts a discrete wavelet transform to construct the adaptive threshold. Although its average deviation is lower than Triggering Method A's, its inference time is the longest among all methods. Only the proposed approach can effectively achieve fault triggering for each sample in the test sets, while the action rates of the other two methods are lower than that of the proposed approach.

Table 6

Performance evaluation for diverse triggering methods

Comparison Method	Action Rate	Average Deviation	Inference Time
1D-UNet	100%	-0.23 ms	15.78 ms
Triggering Method A	79.7%	59.37 ms	<0.65 ms
Triggering Method B	71.5%	4.77 ms	62.92 ms

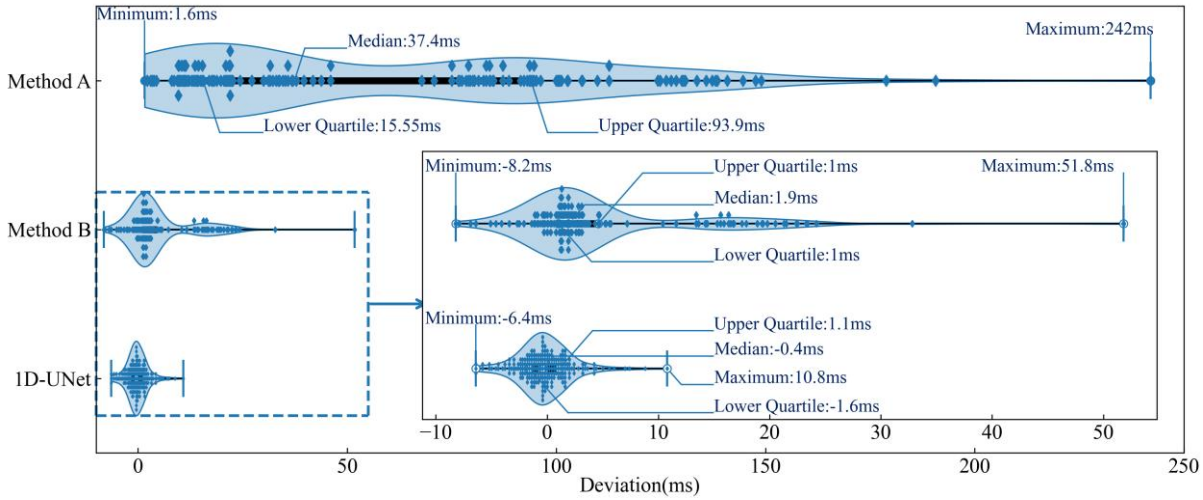

Fig. 16. Triggering deviation of diverse triggering methods.

2) *Fault Detection Stage*: To demonstrate the excellent characteristics of ResNet18 for fault detection, we also constructed GoogLeNet and AlexNet, commonly used models in image recognition, and compared their performance with that of ResNet18 in classifying images with different SE and HMS. The comparison of accuracy and inference time is presented in Table 7. The results in Table 4 indicate that ResNet18 significantly outperforms the other models in terms of accuracy. Despite requiring more time for inference, ResNet18 still satisfies the requirements for fault removal, implying that it is practical for engineering applications.

Table 7

Performance evaluation for diverse AI models

Comparison Model	Accuracy	Inference Time
ResNet18	0.965	49.16 ms
GoogLeNet	0.948	34.58 ms
AlexNet	0.911	12.99 ms

3) *Comprehensive Comparison:*

Several methods from recent literature (Gao et al., 2022; Gautam & Brahma, 2013; Guo et al., 2023; Lima et al., 2018) were implemented as comparative benchmarks to compare the proposed approach and the state-of-the-art techniques comprehensively. As delineated in Section 1, these comparative methods can be bifurcated into two groups: threshold-based and artificial intelligence (AI)-based. The first three sources pertain to threshold-based methods, emphasizing signal analysis within the time, frequency, and time-frequency domains. Owing to the limited availability of well-trained AI models for HIF diagnosis, a recently published model from the literature (Guo et al., 2023) was employed as the AI-based benchmark for comparison with the proposed approach. Table 8 presents a comparative analysis of the results obtained from the proposed method and the state-of-the-art techniques.

As demonstrated in Table 8, the proposed approach achieved an accuracy of 0.965, surpassing the other four comparison methods. The proposed value in (Gautam & Brahma, 2013) was adopted as the threshold of CODO for HIF detection, but its accuracy only reached 0.635, inconsistent with the reported results in the literature. The fixed threshold relies on the system's normal operating condition and only functions in specified distribution systems for threshold-based methods.

In the literature, as presented in (Lima et al., 2018) and (Gao et al., 2022), the respective threshold values are adaptive and suitable for most fault situations. It should be emphasized that the thresholds in (Lima et al., 2018) and (Gao et al., 2022) have been fine-tuned to achieve optimal performance. Finally, the HIF detection accuracy of the methods proposed (Lima et al., 2018) and (Gao et al., 2022) reached 0.812 and 0.807, respectively. These values surpassed the accuracy reached by the method proposed in the literature (Gautam & Brahma, 2013) yet remained inferior to the results obtained through the approach proposed in this study.

The AI model in literature (Guo et al., 2023) was considered the AI-based benchmark, an end-to-end model focusing on the zero-crossing phenomenon present in zero-sequence current. The analysis in Section 2 reveals that the zero-sequence current measured far from the actual fault point may exhibit fewer irregularities than the actual fault current of HIF, explaining why the AI model in (Guo et al., 2023) only attained an

accuracy of 0.699. The proposed approach integrated 1D-UNet and ResNet18 to facilitate fault triggering and detection, achieving an optimal accuracy of 0.965 for HIF diagnosis.

Table 8
Comparison results with the current state of the art

Comparison Literature	Method Category	Analysis Domain	Electrical Quantity	Accuracy
(Gautam & Brahma, 2013)	Threshold-based	Time Domain	Phase Voltage	0.635
(Lima et al., 2018)	Threshold-based	Frequency Domain	Phase Current	0.812
(Gao et al., 2022)	Threshold-based	Time-frequency Domain	Zero-sequence Current	0.807
(Guo et al., 2023)	AI-based	Time Domain	Zero-sequence Current	0.699
Proposed Approach	AI-based	Time Domain, Frequency Domain	Zero-sequence Voltage	0.965

4.3. Engineering Deployment

In this work, we have developed a prototype for real-time diagnosis in engineering applications, which can be installed in substations and distribution feeders. The prototype's architecture is depicted in Fig. 17, comprising an acquisition module and a processing module. The former is based on an STM32 microcontroller, responsible for analog to digital conversion and data transmission to the processing module. The processing module is based on NVIDIA Jetson TX2, equipped with graphics processing units (GPUs) for data inference.

The feasibility of real-time diagnosis depends on the inference speed of the proposed approach on specific hardware. To evaluate the prototype's performance, we calculated the proposed approach's inference time on the developed prototype and listed it in Table 9. The results indicate that the inference time of the proposed approach on the developed prototype is almost the same as that on a personal computer, which meets the requirements of real-time diagnosis. Thus, the developed prototype embedded with the proposed approach can achieve a real-time diagnosis of HIF.

Table 9
Inference time of the developed prototype

Stage	Inference Time
Fault Triggering	18.86 ms
Fault Detection	53.26 ms

To validate the effectiveness of the developed prototype, we used the protection relay tester to play back the waveform of field recordings. Furthermore, we connected the tester and the prototype for data acquisition and processing. The workflow of the developed prototype is shown in Fig. 18. The monitoring devices, such as the fault terminal unit, collect field faults in distribution networks. Typically, the collected data is stored in COMTRADE format, which can be recreated by the protection relay tester and input into our developed prototype for fault triggering and fault detection.

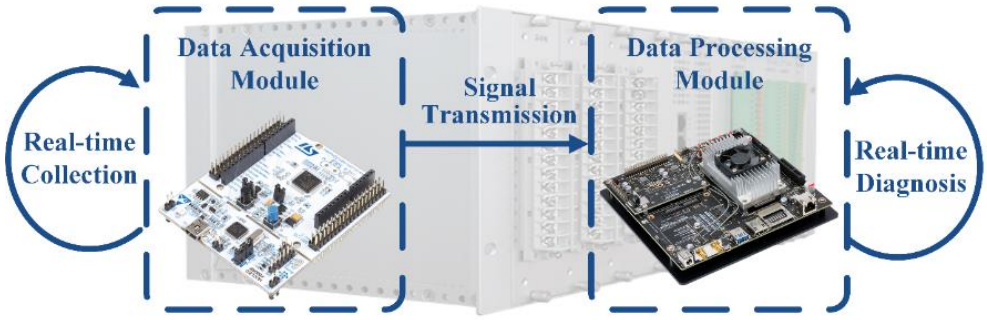

Fig. 17. Architecture of the developed prototype

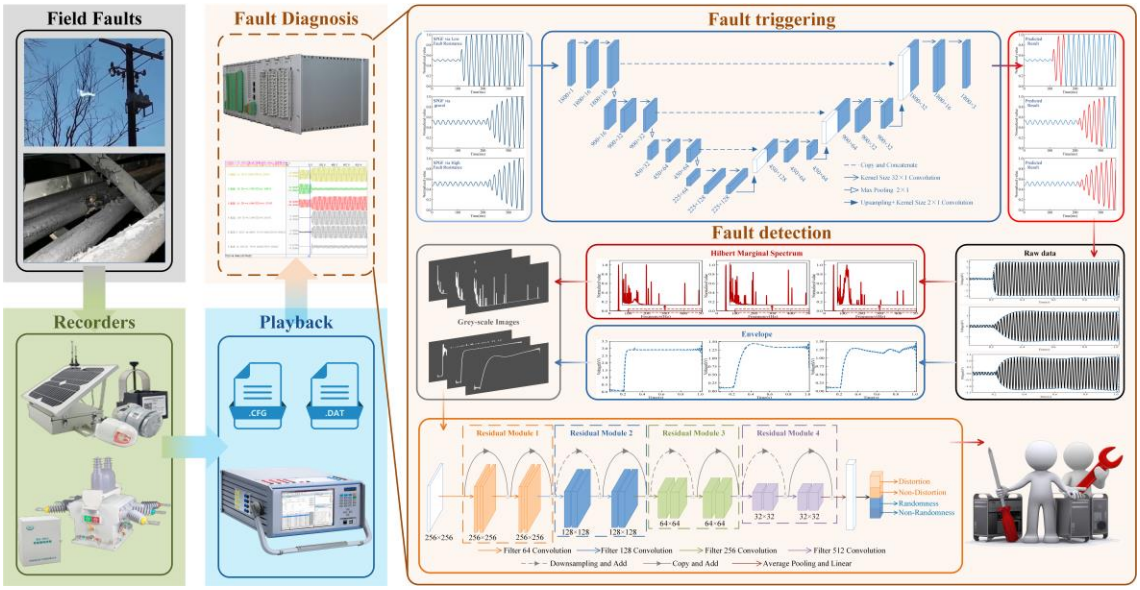

Fig. 18. Workflow of the developed prototype

5. Conclusions

Regarding fault triggering and detection, we have proposed a novel semantic-segmentation-based approach using SE and HMS to achieve a real-time diagnosis of HIF. To our knowledge, this is the first paper to use a semantic segmentation model to implement pixel-wise fault triggering and fault inception determination. Our approach leverages the 1D-UNet to predict each sampling point in the zero-sequence voltage, which enables us to locate the transient process of suspected fault events and determine the moment of fault inception. We also extract SE and HMS using the Hilbert-Huang transform, which represents the distortion and randomness of HIF characteristics, respectively. To detect the type of suspected fault event, we employ the ResNet18, which confirms the existence of HIF based on the distortion and randomness characteristics. We have developed an industrial prototype embedded with our proposed diagnostic approach. Our experimental results show that it achieves high accuracy and efficiency in HIF diagnosis, demonstrating its potential for future applications.

CRediT authorship contribution statement

Jian-Hong Gao: Conceptualization, Methodology, Writing-Original draft preparation. **Mou-Fa Guo:** Supervision, Validation. **Shuyue Lin**: Reviewing and Editing. **Duan-Yu Chen**: Software, Data curation

Declaration of competing interest

The authors declare that they have no known competing financial interests or personal relationships that could have appeared to influence the work reported in this paper.

Acknowledgments

This work was supported in part by the National Natural Science Foundation of China through the Project of Research of Flexible and Adaptive Arc-Suppression Method for Single-Phase Grounding Fault in Distribution Networks under Project 51677030.

References

Aziz, M. S. A., Hassan, M. A. M., & Zahab, E. A. (2012). High-impedance Faults Analysis in Distribution Networks Using an Adaptive Neuro Fuzzy Inference System. *Electric Power Components and Systems*, *40*(11), 1300-1318. https://doi.org/10.1080/15325008.2012.689418

Bao, Y., Soltanian-Zadeh, S., Farsiu, S., & Gong, Y. (2021). Segmentation of Neurons from Fluorescence Calcium Recordings Beyond Real-time. *Nat Mach Intell*, *3*(7), 590-600. https://doi.org/10.1038/s42256-021-00342-x

Biswal, M., Ghore, S., Malik, O. P., & Bansal, R. C. (2021). Development of Time-Frequency Based Approach to Detect High Impedance Fault in an Inverter Interfaced Distribution System. *IEEE Transactions on Power Delivery*, *36*(6), 3825-3833. https://doi.org/10.1109/tpwrd.2021.3049572

Biswal, M., Mishra, M., Sood, V. K., Bansal, R. C., & Abdelaziz, A. Y. (2022). Savitzky-Golay Filter integrated matrix pencil method to identify high impedance fault in a renewable penetrated distribution system. *Electric Power Systems Research*, *210*, 108056. https://doi.org/10.1016/j.epsr.2022.108056

Biswal, T., & Parida, S. K. (2022). A novel high impedance fault detection in the micro-grid system by the summation of accumulated difference of residual voltage method and fault event classification using discrete wavelet transforms and a decision tree approach. *Electric Power Systems Research*, *209*, 1-17. https://doi.org/10.1016/j.epsr.2022.108042

Chaitanya, B. K., Yadav, A., & Pazoki, M. (2019). An intelligent detection of high-impedance faults for distribution lines integrated with distributed generators. *IEEE Systems Journal*, *14*(1), 870-879.

Gao, J., Wang, X., Wang, X., Yang, A., Yuan, H., & Wei, X. (2022). A High-Impedance Fault Detection Method for Distribution Systems Based on Empirical Wavelet Transform and Differential Faulty Energy. *IEEE Transactions on Smart Grid*, *13*(2), 900-912. https://doi.org/10.1109/tsg.2021.3129315

Gautam, S., & Brahma. (2013). Detection of High Impedance Fault in Power Distribution Systems Using Mathematical Morphology. *IEEE Transactions on Power Systems*, *28*(2), 1226-1234. https://doi.org/10.1109/tpwrs.2012.2215630

Gomes, D. P. S., Ozansoy, C., & Ulhaq, A. (2018). High-Sensitivity Vegetation High-Impedance Fault Detection Based on Signal's High-Frequency

Contents. *IEEE Transactions on Power Delivery*, *33*(3), 1398-1407. https://doi.org/10.1109/tpwrd.2018.2791986

Guo, M.-F., Liu, W.-L., Gao, J.-H., & Chen, D.-Y. (2023). A Data-Enhanced High Impedance Fault Detection Method Under Imbalanced Sample Scenarios in Distribution Networks. *IEEE Transactions on Industry Applications*, 1-14. https://doi.org/10.1109/tia.2023.3256975

Guo, M.-F., Zeng, X.-D., Chen, D.-Y., & Yang, N.-C. (2018). Deep-Learning-Based Earth Fault Detection Using Continuous Wavelet Transform and Convolutional Neural Network in Resonant Grounding Distribution Systems. *IEEE Sensors Journal*, *18*(3), 1291-1300. https://doi.org/10.1109/jsen.2017.2776238

He, K., Zhang, X., Ren, S., & Sun, J. (2016). Deep Residual Learning for Image Recognition. 2016 IEEE Conference on Computer Vision and Pattern Recognition (CVPR),

IEEE Standard for Interconnection and Interoperability of Distributed Energy Resources with Associated Electric Power Systems Interfaces. (2018). *IEEE Std 1547-2018 (Revision of IEEE Std 1547-2003)*, 1-138. https://doi.org/10.1109/ieeestd.2018.8332112

Keng-Yu, L., Shi-Lin, C., Ching-Jung, L., Tzong-Yih, G., Tsair-Ming, L., & Jer-Sheng, S. (1999). Energy variance criterion and threshold tuning scheme for high impedance fault detection. IEEE Power Engineering Society. 1999 Winter Meeting (Cat. No.99CH36233),

Lima, É. M., dos Santos Junqueira, C. M., Brito, N. S. D., de Souza, B. A., de Almeida Coelho, R., & Gayoso Meira Suassuna de Medeiros, H. (2018). High impedance fault detection method based on the short-time Fourier transform. *IET Generation, Transmission, Distribution*, *12*(11), 2577-2584.

Lin, C., Gao, W., & Guo, M. F. (2019). Discrete Wavelet Transform-Based Triggering Method for Single-Phase Earth Fault in Power Distribution Systems. *IEEE Transactions on Power Delivery*, *34*(5), 2058-2068. https://doi.org/10.1109/TPWRD.2019.2913728

Londhe, A. N., & Atulkar, M. (2021). Semantic segmentation of ECG waves using hybrid channel-mix convolutional and bidirectional LSTM. *Biomedical Signal Processing and Control*, *63*, 1-11. https://doi.org/10.1016/j.bspc.2020.102162

Mo, Y., Wu, Y., Yang, X., Liu, F., & Liao, Y. (2022). Review the state-of-the-art technologies of semantic segmentation based on deep learning. *Neurocomputing*, *493*, 626-646. https://doi.org/10.1016/j.neucom.2022.01.005

Oh, S. L., Ng, E. Y. K., Tan, R. S., & Acharya, U. R. (2019). Automated beat-wise arrhythmia diagnosis using modified U-net on extended electrocardiographic recordings with heterogeneous arrhythmia types. *Comput Biol Med*, *105*, 92-101. https://doi.org/10.1016/j.compbiomed.2018.12.012

Samantaray, S. R. (2012). Ensemble decision trees for high impedance fault detection in power distribution network. *International Journal of Electrical Power & Energy Systems*, *43*(1), 1048-1055. https://doi.org/10.1016/j.ijepes.2012.06.006

Sarwagya, K., De, S., & Nayak, P. K. (2018). High-impedance fault detection in electrical power distribution systems using moving sum approach. *IET Science, Measurement&Technology*, *12*(1), 1-8.

Shahrtash, S. M., & Sarlak, M. (2006). High Impedance Fault Detection Using Harmonics Energy Decision Tree Algorithm. 2006 International Conference on Power System Technology,

Sheng, Y., & Rovnyak, S. M. (2004). Decision Tree-Based Methodology for High Impedance Fault Detection. *IEEE Transactions on Power Delivery*, *19*(2), 533-536. https://doi.org/10.1109/tpwrd.2003.820418

Silva, S., Costa, P., Gouvea, M., Lacerda, A., Alves, F., & Leite, D. (2018). High impedance fault detection in power distribution systems using wavelet transform and evolving neural network. *Electric Power Systems Research*, *154*, 474-483.

Sirojan, T., Lu, S., Phung, B. T., Zhang, D., & Ambikairajah, E. (2022). Sustainable Deep Learning at Grid Edge for Real-Time High Impedance Fault Detection. *IEEE Transactions on Sustainable Computing*, *7*(2), 346-357. https://doi.org/10.1109/tsusc.2018.2879960

Wang, B., & Cui, X. (2022). Nonlinear Modeling Analysis and Arc High-Impedance Faults Detection in Active Distribution Networks With Neutral Grounding via Petersen Coil. *IEEE Transactions on Smart Grid*, *13*(3), 1888-1898. https://doi.org/10.1109/tsg.2022.3147044

Wang, B., Geng, J., & Dong, X. (2018). High-Impedance Fault Detection Based on Nonlinear Voltage–Current Characteristic Profile Identification. *IEEE Transactions on Smart Grid*, *9*(4), 3783-3791. https://doi.org/10.1109/tsg.2016.2642988

Wang, X.-F., Huang, D.-S., & Xu, H. (2010). An efficient local Chan–Vese model for image segmentation. *Pattern Recognition*, *43*(3), 603-618. https://doi.org/10.1016/j.patcog.2009.08.002

Wang, X., Gao, J., Wei, X., Song, G., Wu, L., Liu, J., Zeng, Z., & Kheshti, M. (2019). High Impedance Fault Detection Method Based on Variational Mode Decomposition and Teager–Kaiser Energy Operators for Distribution Network. *IEEE Transactions on Smart Grid*, *10*(6), 6041-6054. https://doi.org/10.1109/tsg.2019.2895634

Wang, X., Wei, X., Gao, J., Song, G., Kheshti, M., & Guo, L. (2022). High-Impedance Fault Detection Method Based on Stochastic Resonance For a Distribution Network With Strong Background Noise. *IEEE Transactions on Power Delivery*, *37*(2), 1004-1016. https://doi.org/10.1109/tpwrd.2021.3075472

Wang, Y., Zhou, J., Li, Z., Dong, Z., & Xu, Y. (2015). Discriminant-Analysis-Based Single-Phase Earth Fault Protection Using Improved PCA in Distribution Systems. *IEEE Transactions on Power Delivery*, *30*(4), 1974-1982. https://doi.org/10.1109/tpwrd.2015.2408814

Wei, M., Liu, W., Shi, F., Zhang, H., Jin, Z., & Chen, W. (2021). Distortion-Controllable Arc Modeling for High Impedance Arc Fault in the Distribution Network. *IEEE Transactions on Power Delivery*, *36*(1), 52-63. https://doi.org/10.1109/tpwrd.2020.2981376

Xiao, Q.-M., Guo, M.-F., & Chen, D.-Y. (2022). High-Impedance Fault Detection Method Based on One-Dimensional Variational Prototyping-Encoder for Distribution Networks. *IEEE Systems Journal*, *16*(1), 966-976. https://doi.org/10.1109/jsyst.2021.3053769

Yuan, J., & Jiao, Z. (2022). Faulty feeder detection based on fully convolutional network and fault trust degree estimation in distribution networks. *International Journal of Electrical Power & Energy Systems*, *141*, 1-13. https://doi.org/10.1016/j.ijepes.2022.108264

Zhang, C., Zhao, S., & He, Y. (2021). An integrated method of the future capacity and RUL prediction for lithium-ion battery pack. *IEEE Transactions on Vehicular Technology*, *71*(3), 2601-2613.

Zhang, C., Zhao, S., Yang, Z., & Chen, Y. (2022). A reliable data-driven state-of-health estimation model for lithium-ion batteries in electric vehicles. *Frontiers in Energy Research*, *10*.

Zhang, J., He, Z. Y., Lin, S., Zhang, Y. B., & Qian, Q. Q. (2013). An ANFIS-based fault classification approach in power distribution system. *International Journal of Electrical Power & Energy Systems*, *49*, 243-252. https://doi.org/10.1016/j.ijepes.2012.12.005

Zhao, S., Zhang, C., & Wang, Y. (2022). Lithium-ion battery capacity and remaining useful life prediction using board learning system and long short-term memory neural network. *Journal of Energy Storage*, *52*, 104901. https://doi.org/10.1016/j.est.2022.104901